

Internal Structure of the 2019 April 2 CME

Brian E. Wood¹, Carlos R. Braga², Angelos Vourlidas³

ABSTRACT

We present the first analysis of internal coronal mass ejection (CME) structure observed very close to the Sun by the Wide-field Imager for Solar PRobe (WISPR) instrument on board Parker Solar Probe (PSP). The transient studied here is a CME observed during PSP’s second perihelion passage on 2019 April 2, when PSP was only 40 R_{\odot} from the Sun. The CME was also well observed from 1 au by the STEREO-A spacecraft, which tracks the event all the way from the Sun to 1 au. However, PSP/WISPR observes internal structure not apparent in the images from 1 au. In particular, two linear features are observed, one bright and one dark. We model these features as two loops within the CME flux rope channel. The loops can be interpreted as bundles of field lines, with the brightness of the bright loop indicative of lots of mass being loaded into those field lines, and with the dark loop being devoid of such mass loading. It is possible that these loops are actually representative of two independent flux rope structures within the overall CME outline.

Subject headings: Sun: coronal mass ejections (CMEs) — solar wind — interplanetary medium

1. Introduction

Launched in 2018, Parker Solar Probe (PSP) is currently exploring the origins of the solar wind, venturing closer to the Sun than any previous spacecraft. This exploration uses primarily a suite of in situ particle and field instruments, designed to directly measure plasma and field properties. However, PSP also has an imaging instrument on board, the Wide-field Imager for Solar PRobe (WISPR) (Vourlidas et al. 2016). The two heliospheric imagers that constitute PSP/WISPR observe white light scattered from the solar wind in the ram direction of PSP’s orbit.

In addition to exploring the quiescent solar wind, the PSP instruments have also observed a number of transients that have happened to occur near PSP’s perihelion passages. In PSP’s first perihelion passage, WISPR observed two noteworthy coronal mass ejections (CMEs). The first was

¹Naval Research Laboratory, Space Science Division, Washington, DC 20375, USA; brian.wood@nrl.navy.mil

²George Mason University, 4400 University Drive, Fairfax, VA 22030, USA

³The Johns Hopkins University Applied Physics Laboratory, Laurel, MD 20723, USA

on 2018 November 1, characterized by a small circular cavity indicative of a magnetic flux rope (FR) viewed edge-on (Hess et al. 2020; Rouillard et al. 2020). The second was a jet-like streamer blob event, which was observed even closer to perihelion on 2018 November 5. This event was not only observed by WISPR but also by coronagraphs on two spacecraft operating at 1 au: the C2 and C3 constituents of the Large Angle and Spectrometric COronagraph (LASCO) instrument on board the SOlar and Heliospheric Observatory (SOHO), and the COR2-A coronagraph on the Solar TERrestrial RELations Observatory (STEREO). This provided the first opportunity for a full morphological reconstruction of a WISPR-observed CME utilizing three distinct vantage points (Wood et al. 2020).

On 2019 April 1-2, during PSP’s second perihelion passage, WISPR observed two larger CMEs than the ones seen the previous orbit (Braga & Vourlidas 2021). The events were also observed by STEREO-A and SOHO/LASCO. The first analyses of these CMEs focused on measuring their trajectory directions and kinematic properties, in order to demonstrate consistency between measurements made from WISPR images and those from 1 au (Liewer et al. 2020; Braga & Vourlidas 2021). However, the April 2 CME is also noteworthy for having an unusual appearance in the WISPR images, which Liewer et al. (2020) referred to as “skull-like.” This curious visage is not apparent in the images from the 1 au spacecraft, meaning that this is an opportunity to study CME internal structure with PSP/WISPR that is only visible thanks to PSP’s close proximity to the CME near the Sun. Although there have already been morphological reconstructions of overall CME shapes using PSP/WISPR (Rouillard et al. 2020; Wood et al. 2020), this is the first attempt to reconstruct internal CME structure from WISPR images.

2. Observations

The second perihelion passage of PSP brought the spacecraft within $35.4 R_{\odot}$ of the Sun at UT 22:40 on 2019 April 4. The CME that is the focus of our study was first seen by the WISPR instrument two days earlier at about UT 11:00 on 2019 April 2, with PSP $40.0 R_{\odot}$ from the Sun. The viewing geometry is illustrated in Figure 1, which shows the positions of PSP, STEREO-A, and Earth relative to the CME trajectory, in heliocentric Earth ecliptic (HEE) coordinates. The fields of view of six white light telescopes that image the CME are also shown. This includes the C3 coronagraph component of SOHO/LASCO, operating near Earth, which observes the corona at Sun-center distances in the plane-of-sky of $3.7\text{--}30 R_{\odot}$ (Brueckner et al. 1995). The trajectory of the 2019 April 2 CME is perfectly placed for tracking with STEREO-A. The STEREO-A observations include ones from the COR2-A coronagraph, observing at angular distances from Sun-center of $0.7^{\circ}\text{--}4.2^{\circ}$ ($2.5\text{--}15.6 R_{\odot}$), and also the HI1-A and HI2-A heliospheric imagers, viewing at $3.9^{\circ}\text{--}24.1^{\circ}$ and $19^{\circ}\text{--}89^{\circ}$, respectively (Howard et al. 2008; Eyles et al. 2009). Finally, Figure 1 also depicts the fields of view of WISPR’s two heliospheric imagers: WISPR-I, imaging at $13^{\circ}\text{--}53^{\circ}$ from the Sun, and WISPR-O, imaging at $50^{\circ}\text{--}108^{\circ}$ (Vourlidas et al. 2016).

The 2019 April 2 CME probably traces its origins to AR12737, a newly born active region that

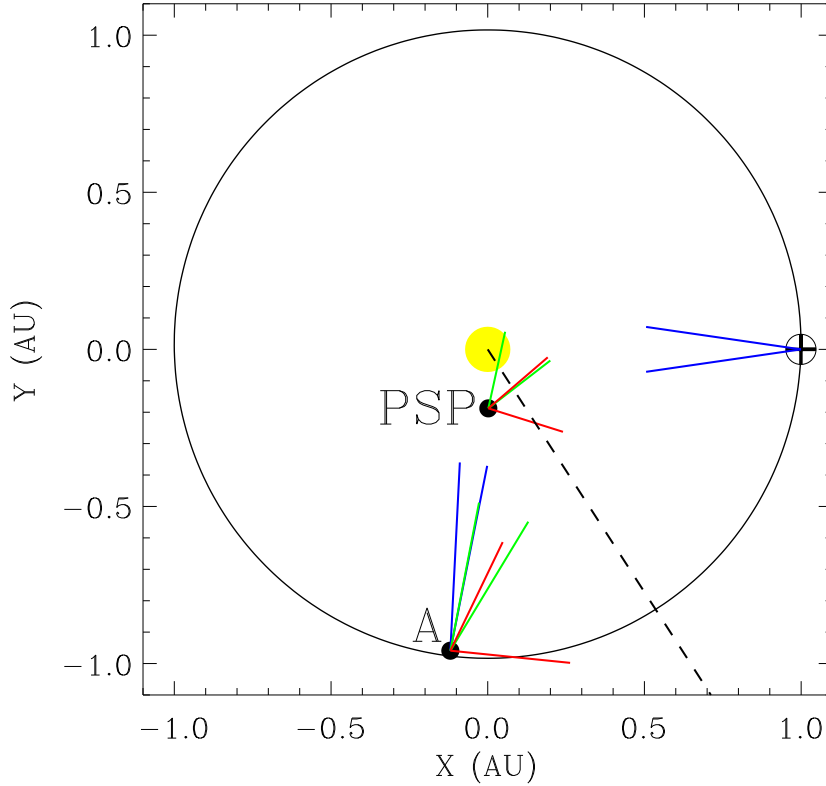


Fig. 1.— The positions of Earth, PSP, and STEREO-A in the ecliptic plane on 2019 April 2 (in HEE coordinates). At PSP’s position, the green and red lines indicate the fields of view of the WISPR-I and WISPR-O detectors. At Earth’s position, the blue lines indicate the field of view of the LASCO/C3 coronagraph on SOHO. At STEREO-A’s position, the blue, green, and red lines indicate the fields of view of COR2-A, HI1-A, and HI2-A. The dashed line indicates the central trajectory of the 2019 April 2 CME observed by all these imagers.

emerges at about UT 09:00 on 2019 March 31, as seen in images from the Atmospheric Imaging Assembly (AIA) instrument on the Solar Dynamics Observatory (SDO). This active region has already received attention for being the likely origin of persistent Type III radio bursts observed by PSP during its second perihelion passage (Harra et al. 2021; Brooks et al. 2021). Given that the trajectory inferred for the April 2 CME traces back to near AR12737 (Liewer et al. 2020), a likely cause of the CME is the destabilization of the local streamer belt due to the emergence and expansion of AR12737. However, there is some ambiguity whether it is proper to call AR12737 the CME “source region,” as there is little actual surface activity associated with the eruption. There is no flare and no filament eruption, for example. The only surface activity that might be directly connected to the CME is a small coronal dimming event apparent in 171 Å SDO/AIA images, which occurs NW of AR12737 at UT 19:11 on April 1.

Figures 2-5 show a selection of images of the CME, from all six of the aforementioned white light telescopes. The WISPR images in Figures 2-3 are shown after subtraction of an average

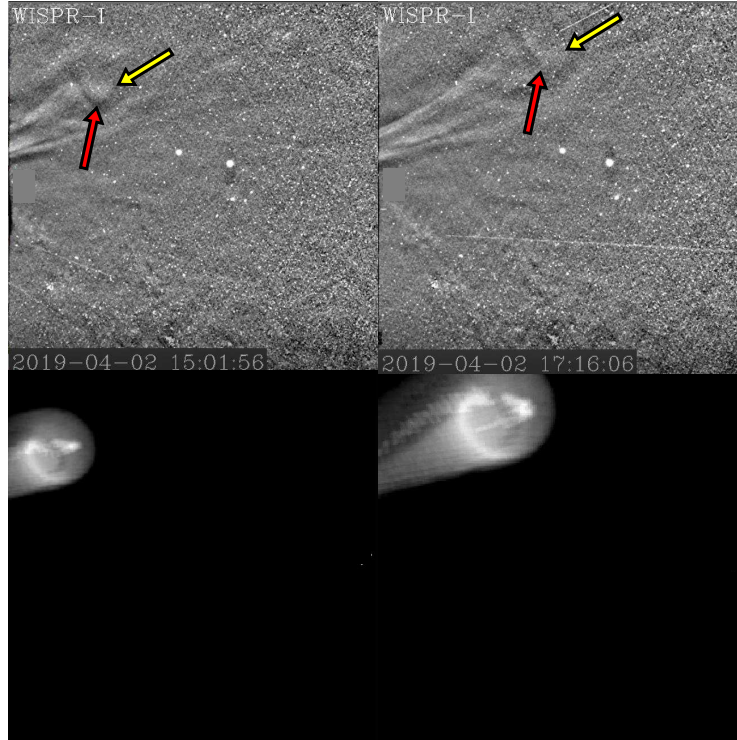


Fig. 2.— Two images of the 2019 April 2 CME from the WISPR-I detector on of the WISPR instrument on PSP. Yellow arrows point to the top of a bright internal structure that we identify as Loop 1, and red arrows point to a dark internal linear structure that we identify as Loop 2 (see Section 4). Synthetic images of the event are shown below the real images, based on the 3-D reconstruction described in Section 4. A movie version of this figure is available online.

image, in order to remove static structure and focus attention on the transient emission. The STEREO-A and LASCO/C3 images in Figures 4-5 are running difference images, with the prior image subtracted from each image, once again to emphasize transient emission. It is worth noting that each of Figures 2-5 are accompanied by movie versions available in the online article, which display the CME far better and more comprehensively than static images can.

The details of the CME are best seen in the WISPR-I images in Figure 2. The outline of the top of the CME is a roughly circular cavity suggestive of an FR channel observed edge-on. Inside the cavity is a bright, linear feature, which stretches back toward the Sun, the top of which is marked by a yellow arrow in Figure 2. Even more unusual is a dark, linear feature superposed onto the bright feature, oriented perpendicular to the CME’s propagation direction, marked by a red arrow in Figure 2. It is the combination of these two features that give the CME what Liewer et al. (2020) describe as a “skull-like” appearance. Interpreting this internal structure is the primary goal of our study.

This internal structure is only apparent in the WISPR-I images. In the images from 1 au (see



Fig. 3.— On the left is a PSP/WISPR-O image of the 2019 April 2 CME, with the CME only faintly visible in the upper left corner of the image, and on the right is a synthetic image of the event based on the 3-D reconstruction described in Section 4. The CME is far more visible in the movie version of this figure, which is available online.

Figures 4-5), the CME is simply too faint and far away to discern this internal structure. It should be noted that if we were using those data to study internal structure, we would not be using the running difference technique as we are in Figures 4-5, as the imprint of the shadow of the previous image on each image confuses the internal appearance. In WISPR-O data, the CME skims the top of the field of view (see Figure 3), and only the bottom edge of the CME is really seen. In the analysis described below, the WISPR-O data are nevertheless useful for constraining the proximity of that part of the CME to PSP, as the apparent speed of the CME through the WISPR-O field of view is a sensitive diagnostic to its proximity, with a closer proximity leading to a faster apparent propagation. The WISPR-O data are also notable for having Earth in the field of view, meaning that this is the first reported instance of a telescope near the Sun looking back toward Earth and seeing a CME propagating through the interplanetary space in between, as illustrated in Figure 1.

3. Kinematics

Our primary goal is to model the internal structure of the 2019 April 2 CME, but there are several intermediate steps on the way to that final goal. One is to have a full 3-D morphological model of the overall CME outline, within which the internal structure can be placed. Another is to have a full kinematic model for the CME, so that we can properly match the appearance of the

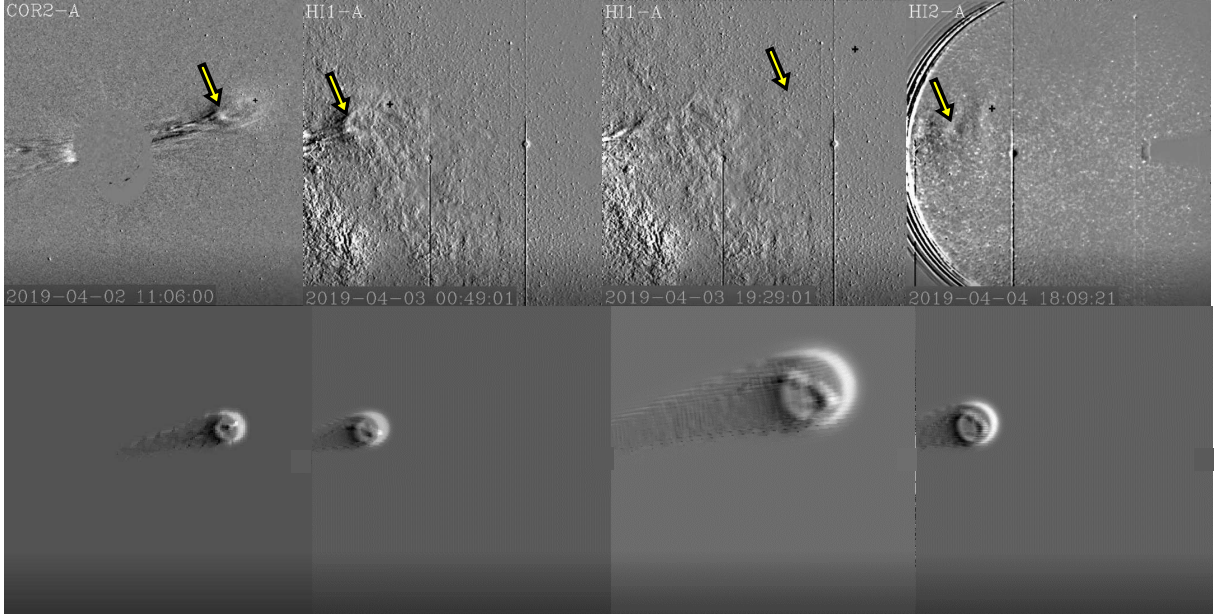


Fig. 4.— A sequence of four images of the 2019 April 2 CME from the STEREO-A spacecraft, one from COR2-A, two from HI1-A, and one from HI2-A. A small black plus sign marks the position of the CME leading edge as predicted by the kinematic model of the CME described in Section 3. Yellow arrows point to a bright pileup region at the back end of the CME flux rope channel caused by a fast ambient wind coming from behind. Synthetic images of the event are shown below the real images, based on the 3-D reconstruction described in Section 4.

CME in all the telescope fields of view at all times.

The CME kinematics have already been extensively studied by Liewer et al. (2020) and Braga & Vourlidas (2021). However, these analyses focused on the use of this CME to test techniques for measuring CME kinematics from WISPR images. We present here a kinematic model of the event applicable for the full time range of available observations. It is actually STEREO-A that is by far the best platform for studying this CME’s kinematics, as STEREO-A tracks the event continuously from near the Sun all the way to 1 au. Our kinematic analysis therefore focuses on STEREO-A data.

From COR2-A, HI1-A, and HI2-A images, we measure the elongation angle, ϵ , of the leading edge of the CME as a function of time. Converting ϵ to actual distances from Sun-center, r , requires assumptions about the shape of the CME front. Consistent with past analyses (Wood et al. 2017, 2020), we use the so-called “harmonic mean” approximation from Lugaz et al. (2009),

$$r = \frac{2d \sin \epsilon}{1 + \sin(\epsilon + \phi)}, \quad (1)$$

where d is the distance from STEREO-A to the Sun and ϕ is the angle between the CME’s central trajectory and the STEREO-A/Sun line. This essentially approximates the CME as a sphere centered halfway between the Sun and the CME’s leading edge. Based on the morphological analysis

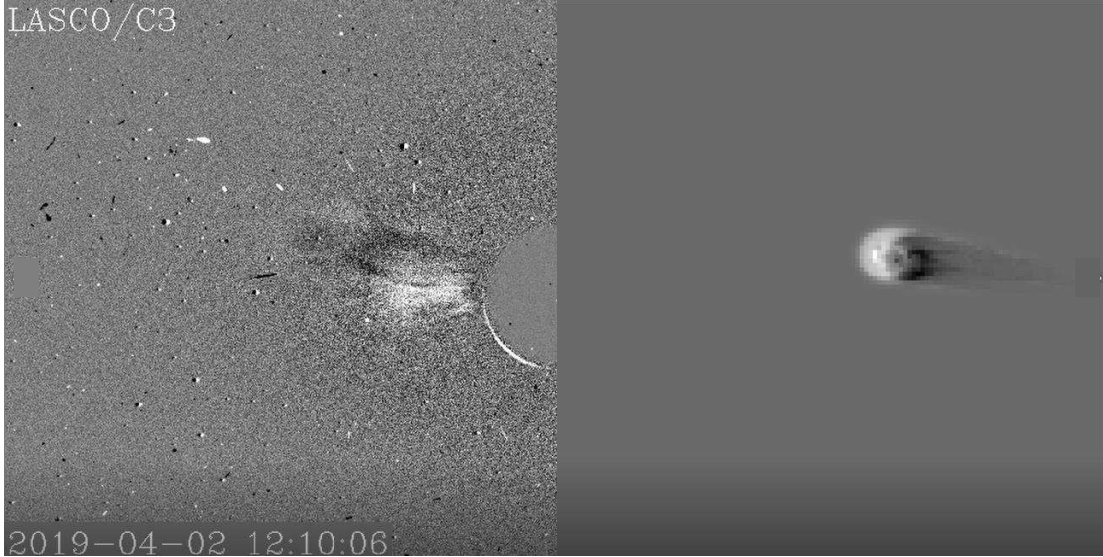


Fig. 5.— On the left is a LASCOC3 image of the 2019 April 2 CME, and on the right is a synthetic image of the event based on the 3-D reconstruction described in Section 4. A movie version of this figure is available online.

described in the next section, we infer a trajectory direction of $\phi = 41^\circ$ relative to STEREO-A, and the measured elongation angles then translate to the CME leading edge distances shown in the top panel of Figure 6.

In order to infer a velocity profile for the CME, we fit a simple two-phase kinematic model to the data, assuming a phase of constant acceleration followed by a phase of constant velocity. In the resulting fit in Figure 6, the CME accelerates at a rate of 6.7 m s^{-2} for about 13 hours before leveling out at a final speed of 420 km s^{-1} . These acceleration and speed measurements are in excellent agreement with the $6.667 \pm 2.714 \text{ m s}^{-2}$ and $432 \pm 51 \text{ km s}^{-1}$ values reported by Braga & Vourlidas (2021), who also find that the acceleration is over by the time the CME reaches the HI1-A field of view.

4. Morphological Reconstruction

The goal in this section is to model the 3-D structure of the CME, including the internal structure, but we start by modeling the outline of the overall CME assuming an FR shape. For this purpose, we use well-established techniques that have already been applied extensively in the study of CMEs observed by SOHO, STEREO, and PSP (Wood & Howard 2009; Wood et al. 2017, 2020). The construction of an FR shape begins with the definition of loops that constitute the inner and outer edges of a 2-D FR in an xy-plane with the x-axis pointing through the apex of the

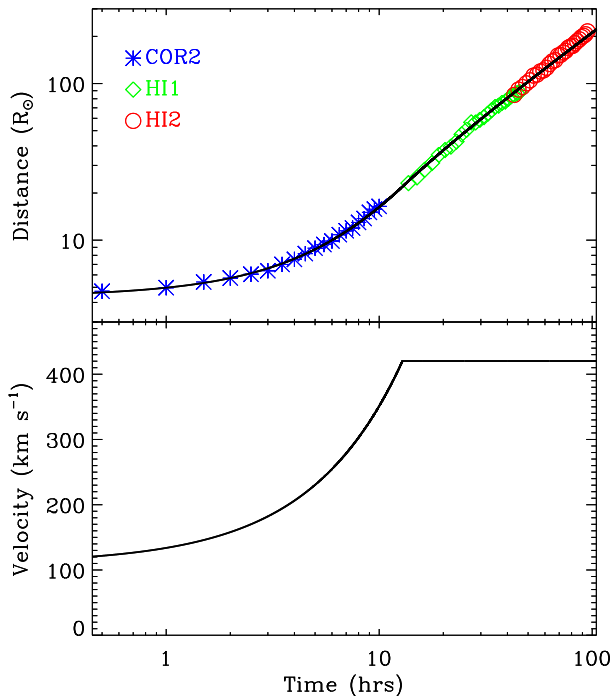


Fig. 6.— The top panel shows distance measurements for the leading edge of the 2019 April 2 CME as a function of time based on images from STEREO-A, specifically COR2-A (blue asterisks), HI1-A (green diamonds), and HI2-A (red circles). The $t = 0$ point on the time axis corresponds to UT 03:06 on April 2. These data points are fitted with a simple kinematic model assuming a constant acceleration phase followed by a constant velocity phase. The solid line is the best fit, and the bottom panel shows the inferred velocity profile.

FR. In polar coordinates in this plane, these two loops can be expressed as

$$r(\theta) = r_{max} \exp \left(-\frac{1}{2} \left| \frac{\theta}{\sigma} \right|^{\alpha_s} \right). \quad (2)$$

The σ parameter determines the widths of the loops, which can also be described by a full-width-at-half-maximum,

$$FWHM_s = 2 (1.386)^{1/\alpha_s} \sigma. \quad (3)$$

The α_s parameter controls the shape of the top of the loop.

We have to define the electron density distribution for the 2-D FR, as the ultimate goal is to create synthetic images of the CME from a density cube containing the final 3-D FR shape. In the past, we have placed mass only on the surface of the FR, leaving the interior empty, as we were only interested in the outline of the CME shape. However, we are here interested in the internal structure as well, so we change our approach. We start by assuming a uniform density inside the FR, $n_1(x, y) = n_{FR}$. The densities of the internal structures described below will be defined relative to this baseline density. The absolute value of n_{FR} is actually unimportant for our purposes, as we are only comparing the general appearance of the CME structure in the real and synthetic

Table 1: CME Morphological Parameters

Parameter	Description	FR	Loop 1	Loop 2
λ_s (deg)	Trajectory longitude	-57	-57	-57
β_s (deg)	Trajectory latitude	10	10	10
γ_s (deg)	Tilt angle	8
FWHM_s (deg)	Angular width	48.4	30.4	19.4
Λ_s	Aspect ratio	0.096	0.027	0.027
η_s	Ellipticity	1.0	1.0	1.0
α_s	Leading Edge Shape	2.5	4.0	4.0
x_{max}	Leading Edge Dist.	1.0	0.95	0.95
<u>Parameters for Computing γ_s</u>				
γ_{base} (deg)	Base γ_s	...	25	25
γ_1 (deg)	Initial top γ_s	...	20	-15
γ_2 (deg)	Final top γ_s	...	-20	-75
ξ	Writhe index	...	3.5	3.5
t_0 (hr)	Midpoint time	...	12	12
t_r (hr)	Relaxation time	...	4	4

images, and we are not attempting to make our synthetic images match observed brightness values quantitatively.

The density is then made distance dependent, assuming

$$n_2(x, y) = n_1(x, y) \left(\frac{x}{x_{max}} \right)^\beta, \quad (4)$$

where x_{max} is the distance to the leading edge of the FR from Sun-center along the x-axis (Wood & Howard 2009; Wood et al. 2010). If we maintained constant density (e.g., $\beta = 0$), the legs of the model CME would end up looking brighter in synthetic images than the top of the CME, since the legs are closer to the Sun and therefore scatter more light. This is not consistent with the appearance of CMEs in images. We correct for this by assuming that density increases with distance. Specifically, we assume $\beta = 3$, although the precise value of β is relatively unimportant, since as already noted we are not attempting to quantitatively match observed brightness values.

With the 2-D FR and its density map established, the two loops of the FR are then used to define a 3-D FR shape and density distribution by assuming a circular cross section for the FR, bounded by the two loops. By stretching the FR in the direction perpendicular to the FR creation plane, i.e. the z-axis, an FR can be created with an arbitrary ellipticity, with density independent of z. The 3-D FR is then rotated into the desired orientation in an HEE coordinate system. Adjusting the various quantities involved in the FR creation process allows experimentation with different shapes and orientations.

Once a density cube is prepared, synthetic images are generated using a white-light rendering routine to perform the necessary calculations of Thomson scattering within the density cube

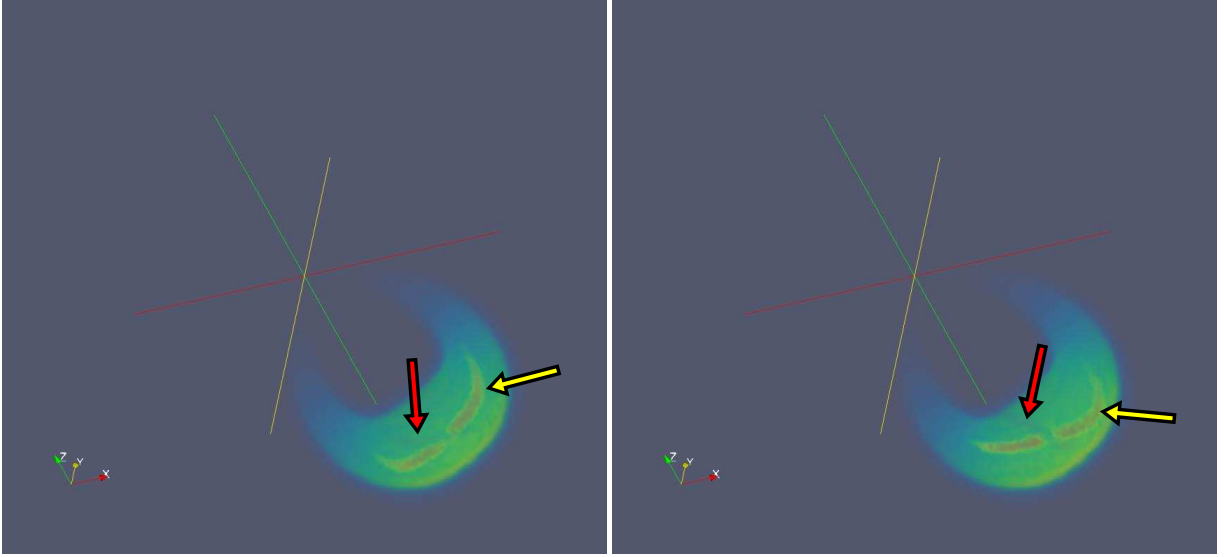


Fig. 7.— Reconstructed 3-D FR structure of the CME observed by *PSP*/WISPR on 2019 April 2, shown in HEE coordinates. The reconstruction includes two loops inside the FR, the high density Loop 1 (yellow arrow) and the low density Loop 2 (red arrow). The loops rotate with time, and the right and left panels show the structure at the beginning and end of the rotation, respectively.

(Billings 1966; Thernisien et al. 2006). The FR is assumed to expand in a self-similar expansion, meaning its shape does not change with time, although this will not be strictly true for the internal structure described below. The expansion of the CME is described by the kinematic model in Figure 6. In this way, we compute synthetic images of the CME for comparison with the images from STEREO-A, PSP/WISPR, and SOHO/LASCO. Parameters of the FR are adjusted to maximize agreement between the real and synthetic images. This is done by trial-and-error, and subjective judgment is used to decide what is the best fit. The primary parameters of interest are listed in Table 1. Figure 7 shows the final FR shape that we decide best describes the outline of the CME, and Figures 2-5 show synthetic images computed from this FR for comparison with the real images.

The parameters in Table 1 defining the shape of the FR use the variable names from Wood et al. (2017). Briefly, λ_s and β_s are the central trajectory in HEE coordinates, with the $\lambda_s = -57^\circ$ direction explicitly indicated in Figure 1. The FR trajectory latitude is slightly above the ecliptic, with $\beta_s = 10^\circ$. The γ_s parameter indicates the tilt angle of the FR, with $\gamma_s = 0^\circ$ corresponding to an E-W orientation parallel to the ecliptic, and $\gamma_s > 0^\circ$ indicating an upward tilt of the western leg. With $\gamma_s = 8^\circ$, our FR is close to being oriented E-W. The FWHM_s parameter is the full-width-at-half-maximum angular width of the FR, defined by Eqn. (2). The aspect ratio, Λ_s , indicates the radius of the apex of the FR divided by the distance of the apex from the Sun, and therefore quantifies the thinness of the FR. Our FR reconstruction scheme allows for the possibility of an

elliptical FR channel, but we see no evidence for ellipticity, so $\eta_s = 1.0$. Finally, the α_s parameter from Eqn. (1) defines the shape of the FR leading edge (see Wood & Howard 2009; Wood et al. 2017), with higher values leading to flatter leading edges.

With the overall FR shape determined, we now turn our attention to the internal structure, namely the bright and dark linear features noted in Section 2. We interpret these features as being narrow loop-like structures within the CME, and we attempt to estimate their shapes from the WISPR-I images. We will henceforth refer to the bright and dark loops as Loop 1 and Loop 2, respectively. Since the FR creation procedures described above are already designed to create loop-like structures, we can apply these same routines to modeling Loops 1 and 2. Our best-fit loop parameters are therefore listed in Table 1 alongside the FR parameters. The FR and two internal loops structures defined by the Table 1 parameters are ultimately combined into a single density cube before the white light rendering calculations are made. The internal loops naturally end up being much thinner (i.e., very low Λ_s) than any CME FRs that these routines have been used to model in the past. In order to make Loop 1 bright and Loop 2 dark, within the boundary of Loop 1 we simply increase the ambient density within the FR by a factor of 3, and within the boundary of Loop 2 we simply set the density to zero. The meaning and implications of this density contrast will be addressed in more detail in Sections 5 and 6.

The constraints on the loop properties are more limited than for the FR as a whole, because we only have the WISPR-I images to go by, while for the FR we have the STEREO-A and SOHO/LASCO images as well. One additional constraint is that we naturally require the loops to reside within the CME FR shape that has already been constructed. Thus, their trajectory directions are assumed identical to the FR. With this constraint, we find we can only come close to reproducing the observations if the loops are writhed, i.e. with different rotation at their tops than at their bases. In the mathematical framework described above, this is equivalent to saying that the tilt angle parameter, γ_s , is dependent on distance from the Sun, i.e. $\gamma_s = \gamma_s(x)$. We assume the following parametrized functional form for γ_s :

$$\gamma_s(x) = \gamma_{base} + (\gamma_{top} - \gamma_{base}) \left(\frac{x}{x_{max}} \right)^\xi, \quad (5)$$

where γ_{base} and γ_{top} are the γ_s values at the loop base and top, respectively, and ξ is an additional power law index parameter that affects the degree to which the writhe is focused at the top of the loop.

An additional complication related to γ_s for the two loops is that we believe the WISPR-I movies of the CME indicate rotation of the tops of the loops during their passage through the WISPR-I field of view, particularly the bright Loop 1. Some sense of this can be seen by comparing the two images in Figure 2. This means that γ_s and γ_{top} are actually time-dependent. In order to model this, we assume

$$\gamma_{top}(t) = \gamma_1 + \left[\frac{\gamma_2 - \gamma_1}{2} \right] \left[\tanh \left(\frac{t - t_0}{2t_r} \right) + 1 \right], \quad (6)$$

where γ_1 and γ_2 are the initial and final values of γ_{top} , respectively. The time t_0 is a midpoint time where γ_{top} is halfway between γ_1 and γ_2 , and the relaxation time t_r defines how rapidly the shift from γ_1 to γ_2 occurs. Note that we have used an expression of time-dependence similar to Eqn. (6) in modeling a CME from 2008 June 1 (Wood et al. 2010). In this case, we do not perceive any clear time dependence for the FR itself, only for the two internal loops inside it.

We use trial-and-error to experiment with the various loop parameters to find the best match for the data. The resulting parameters are listed in Table 1. For the loops, the γ_s parameter is space and time-dependent, and is therefore replaced with the six parameters listed at the bottom of the table. For the time parameters, the $t = 0$ time is the same as in Figure 6, UT 03:06 on 2019 April 2. Thus, the $t_0 = 12$ hr time found for both loops corresponds to UT 15:06 on 2019 April 2, which is roughly the time of the first WISPR-I image in Figure 2. A loop parameter not yet mentioned is one that relates the size of the loops relative to the existing FR. This is quantified by x_{max} in Table 1, which is the loop-top distance divided by the leading edge FR distance, which is $x_{max} = 0.95$ for both loops.

The two panels of Figure 7 show the appearance of the two loops within the FR at early and late times, i.e. with $\gamma_{top} = \gamma_1$ and $\gamma_{top} = \gamma_2$, respectively, indicating the degree of rotation that we perceive for the loops. Figure 2 indicates the degree to which the two loop model is able to reproduce the observed internal structure. The agreement is imperfect, but the synthetic images capture the general characteristics of the CME’s appearance well enough to support the two loop interpretation of the CME. Improving the agreement would probably require the use of more complex and asymmetric shapes than are possible with the parametrized forms used here. In the 1 au images in Figures 4-5, the internal CME structure is difficult to make out even in the synthetic images, particularly the dark Loop 2, consistent with our inability to see this structure in the actual images. This is in part an issue of signal-to-noise, as this is not a particularly bright CME as viewed from 1 au, but this is also due to blurring of the very narrow loops, caused by intrinsic resolution and by lengthy exposure times in HI1 and HI2 compared with WISPR-I data.

5. The Origins of the Time Dependence

The cause of the rotation of Loops 1 and 2 is worthy of more discussion. We were initially concerned that this could be an optical illusion caused by the changing perspective of the CME as it passes through the WISPR-I field of view. Ironically, an excellent example of this effect is apparent in the movie of synthetic HI2-A images of the CME (see movie version of Figure 4). The bright Loop 1 is visible in the synthetic images (though not in the real images) and appears to be rotating as it moves through the HI2-A field of view. But this rotation is entirely illusory, because in the model described above, the loop rotation ceases long before the CME enters the HI2-A field of view. The apparent rotation is due to the upper leg of the loop having a faster apparent motion through the field of view than the lower leg due to the upper leg’s closer proximity to STEREO-A. This projection effect combined with the “fish-eye” distortion of the very large HI2-A field of view

leads to the erroneous impression of rotation. We tried many static loop shapes to see if we could induce this effect in the WISPR-I field of view, but we were unable to find a shape that would produce it. The WISPR-I field of view is not as large as HI2-A, and the image distortions are not as strong. Thus, we conclude that the rotation is likely real.

We hypothesize that the cause of the rotation might be forcing on the CME from behind by a faster ambient solar wind. This wind is most apparent in the COR2-A images (see movie version of Figure 4), where a fast flow is seen behind the CME, which is in fact faster than the leading edge of the CME at that point. One apparent consequence of this is that there is a pileup of material on the back side of the FR channel, which makes the trailing edge of the FR channel brighter than the leading edge in the STEREO-A images, as marked by a yellow arrow in Figure 4. In HI1-A, the trailing edge has a distinct V-shaped appearance. A final effect of external forcing on the CME may be a degree of pancaking, seen late in the HI1-A part of the Figure 4 movie and into the HI2-A field of view. Such flattening of CMEs relative to the direction of propagation has been studied previously (e.g., Savani et al. 2011; Kay & Nieves-Chinchilla 2021). This could in principle be considered in our modeling by making the ellipticity of the FR channel (η_s) time dependent, allowing it to increase with time. However, this is happening well after the CME is in the WISPR-I field of view, and is therefore outside the focus of our study.

The usual conception of a CME is of a fast eruption of material plowing through a slower ambient solar wind, but the situation can be reversed for a slow CME like the 2019 April 2 event. This forcing from behind could be responsible for inducing the observed rotation in the internal CME structure, particularly if some of the fast flow seen behind the CME is actually going up the legs of the FR. It is also possible that the brightness of Loop 1 might be due to mass loading into the loop from this fast flow from behind.

The origin of the fast wind could be AR12737, which we have also associated with the origin of the CME (see Section 2). Harra et al. (2021) and Brooks et al. (2021) have studied this active region extensively with Hinode’s EUV Imaging Spectrometer (EIS), focusing on a region of strong blueshifted Fe XII emission on the east side of the active region. They identify this outflow region as the likely source of Type III radio bursts observed by PSP. Such outflow regions beside active regions have been interpreted as being possible sources of solar wind. As such, it is possible that the fast wind flow observed behind the April 2 CME in COR2-A is connected to this outflow region.

6. Interpreting the Internal Structure

We have interpreted the internal structure of the 2019 April 2 CME seen by WISPR-I as being due to two time-dependent writhed loops, one bright (Loop 1) and one dark (Loop 2). The next step is to address the question of what the existence of these loops implies about the nature of CME structure. On this issue there is still significant ambiguity.

We have placed the loops within a CME outline defined by an FR shape. The magnetic FR

paradigm has become the predominant paradigm for CME field structure, with support from both in situ and imaging data (Lepping et al. 1990; Farrugia et al. 1995; Chen et al. 1997; Bothmer & Schwenn 1998; Vourlidas et al. 2013; Vourlidas 2014; Wood et al. 2017). Within this paradigm, our two loops might be interpreted as indicative of field lines within the FR. This is potentially problematic, because we are not necessarily perceiving the field lines to be twisted around a current axis in a helical fashion, as one would expect within the conventional FR picture (for further discussion see Patsourakos et al. 2020).

However, it seems simplistic to interpret Loops 1 and 2 as simple magnetic field lines, as their lateral widths are clearly resolved and too large to represent single field lines. They must instead be collections of field lines. Another interpretation of the loops is that they are in fact separate and independent FRs within the CME outline (or helical field bundles, at least). Support for this interpretation is provided by the many instances of in situ observations of CMEs implying the existence of multiple FRs (Osherovich et al. 1999; Hu et al. 2003; Farrugia et al. 2011; Hu et al. 2021), including one of the first CMEs observed in situ by PSP (Nieves-Chinchilla et al. 2020). Surveys of “magnetic clouds” (MCs) identified in in situ data, such as Lepping et al. (2011, 2015), include numerous instances of MCs close together in time, which could be FRs within the same CME. Of the 28 CMEs studied by Wood et al. (2017), there were three cases that yielded two MCs in the Lepping et al. (2011, 2015) lists instead of just one, suggesting that roughly 10% of CMEs are perceived as having multiple FRs when they happen to encounter a spacecraft.

It is possible that most CMEs actually contain multiple FRs, potentially arising from interactions with ambient flux systems during CME eruption or propagation. Although most spacecraft encounters with CMEs do not perceive this, we would not actually expect that they would, since a single path through a CME will only sample a small part of it. For example, a random track through the reconstruction shown in Figure 7 would be unlikely to hit both Loops 1 and 2 squarely, making it unlikely that a spacecraft encounter with the 2019 April 2 would have been able to discern the presence of both structures. This could help explain the inconsistent FR orientations inferred for certain CMEs that hit multiple spacecraft (Farrugia et al. 2011; Möstl et al. 2012). The different spacecraft might actually be sampling different FRs within the same CME.

The idea that CMEs actually consist of multiple FRs could also resolve a fundamental size discrepancy that seems to exist between FR structures inferred from images and those inferred from in situ data. In a survey of in situ selected events, Wood et al. (2017) find that magnetic cloud encounter times observed near Earth are on average three times shorter than expected based on FR reconstructions from images. If CMEs usually consist of two or more FRs, the CME shape inferred from the images would represent the outline of the combined collection of FRs, while the in situ data would typically only be encountering one of the FRs, thereby explaining the inconsistency.

It would be worthwhile to try to find other CMEs that have internal structure that might also be interpreted as being indicative of multiple FRs, both with WISPR and with white light imagers operating at 1 au. However, the dearth of prior CME studies suggesting such an interpretation

suggests that the 2019 April 2 CME is unusual in this respect. We suspect that what makes it different is the unusual mass loading that seems to be occurring in Loop 1, making it bright in the WISPR-I images, relative to both Loop 2 and the rest of the CME interior. We have hypothesized that perhaps the mass loading is occurring because the footpoints of Loop 1 are at least in part connected to the outflow region to the southeast of AR12737, while Loop 2 and whatever other magnetic elements might exist within the CME are rooted elsewhere. Normally, CME interiors have rather low density, and if there is no density contrast between the internal magnetic structures within a CME, there will be no way to see them. The 2019 April 2 CME may be a rare case with sufficient density contrast to perceive the structures, and we still would not have been able to see this without PSP/WISPR being able to view the CME close to the Sun.

7. Summary

We have analyzed white light images of the 2019 April 2 CME from PSP/WISPR, STEREO-A, and SOHO/LASCO, with a focus on the transient’s internal structure. Our findings are summarized as follows:

1. The CME appears to be caused by the destabilization of the streamer belt by a newly emerged and expanding underlying active region, AR12737.
2. The analysis includes a comprehensive kinematic model for the CME, relying mostly on STEREO-A, which is able to track the CME continuously from the Sun to 1 au. Using all available imaging data we reconstruct the CME’s 3-D morphology assuming an FR shape.
3. In WISPR-I images we see internal structure within the CME that is not apparent in images from the 1 au spacecraft, emphasizing the usefulness of being able to observe CMEs close to the Sun. We interpret the internal CME structure as consisting of two loops within the FR, one bright and one dark. The loops are writhed, and the tops of the loops appear to exhibit rotation within the WISPR-I field of view, meaning that the writhe is increasing with time. We model the time-dependent 3-D structure of the two loops using methodology similar to that used to model the overall CME FR shape.
4. In the STEREO-A images, we see clear evidence for a fast ambient solar wind flow overtaking the CME from behind, resulting in a visible pileup of material on the backside of the FR channel. We speculate that some of this flow may be going up the legs of the CME, and that this could be responsible for the mass loading that makes Loop 1 bright, and also for the increase in writhe of the two loops. This fast flow might be connected to an outflow region observed by Hinode southeast of AR12737.
5. The two-loop reconstruction of the CME’s internal structure remains subject to interpretation, but our favored interpretation is that the two loops are separate FRs, consistent with the

numerous published examples of multiple MCs being detected in situ within the same CME. It is possible that most CMEs possess multiple FRs within them, but the separate structures are rarely perceived in images due to low internal densities or low relative contrast, and they are only occasionally perceived in situ when a spacecraft happens to encounter more than one of the internal FRs in its track through the CME.

Financial support was provided by the Office of Naval Research. *Parker Solar Probe* was designed, built, and is now operated by the Johns Hopkins Applied Physics Laboratory as part of NASA’s Living with a Star (LWS) program (contract NNN06AA01C). We particularly acknowledge the WISPR instrument team, funded by NASA through grant NNG11EK11I. The STEREO/SECCHI data are produced by a consortium of NRL (US), LMSAL (US), NASA/GSFC (US), RAL (UK), UBHAM (UK), MPS (Germany), CSL (Belgium), IOTA (France), and IAS (France). In addition to funding by NASA, NRL also received support from the USAF Space Test Program and ONR. C.R.B. acknowledged support from NASA’s STEREO/SECCHI project (NNG17PP27I). A.V. acknowledges support from NASA grants 80NSSC20K1282 and 80NSSC19K1261.

REFERENCES

- Billings, D. E. 1966. *A Guide to the Solar Corona* (New York: Academic Press)
- Bothmer, V., & Schwenn, R. 1998, *Ann. Geophys.*, 16, 1
- Braga, C. R., & Vourlidas, A. 2021, *A&A*, 650, A31
- Brooks, D. H., Harra, L., Bale, S. D., et al. 2021, *ApJ*, in press (<https://arxiv.org/abs/2106.03318>)
- Brueckner, G. E., Howard, R. A., Koomen, M. J., et al. 1995, *Sol. Phys.*, 162, 357
- Chen, J., Howard, R. A., Brueckner, G. E., et al. 1997, *ApJ*, 490, L191
- Eyles, C. J., Harrison, R. A., Davis, C. J., et al. 2009, *Sol. Phys.*, 254, 387
- Farrugia, C. J., Berdichevsky, D. B., Möstl, C., et al. 2011, *JASTP*, 73, 1254
- Farrugia, C. J., Osherovich, V. A., & Burlaga, L. F. 1995, *JGR*, 100, 12293
- Harra, L., Brooks, D. H., Bale, S. D., et al. 2021, *A&A*, 650, A7
- Hess, P., Rouillard, A. P., Kouloumvakos, A., et al. 2020, *ApJS*, 246, 25
- Howard, R. A., Moses, J. D., Vourlidas, A., et al. 2008, *Space Sci. Rev.*, 136, 67
- Hu, Q., He, W., Qiu, J., Vourlidas, A., & Zhu, C. 2021, *GRL*, 48, e2020GL090630

- Hu, Q., Smith, C. W., & Ness, N. F. 2003, GRL, 30, 1385
- Kay, C., & Nieves-Chinchilla, T. 2021, JGR, 126, 2020JA028911
- Lepping, R. P., Jones, J. A., & Burlaga, L. F. 1990, JGR, 95, 11957
- Lepping, R. P., Wu, C. -C., Berdichevsky, D. B., & Szabo, A. 2011, Sol. Phys., 274, 345
- Lepping, R. P., Wu, C. -C., Berdichevsky, D. B., & Szabo, A. 2015, Sol. Phys., 290, 2265
- Liewer, P. C., Qiu, J., Penteado, P., et al. 2020, Sol. Phys., 295, 140
- Lugaz, N., Vourlidas, A., & Roussev, I. I. 2009, Ann. Geophys., 27, 3479
- Möstl, C., Farrugia, C. J., Kilpua, E. K. J., et al. 2012, ApJ, 758, 10
- Nieves-Chinchilla, T. N., Szabo, A., Korreck, K. E., et al. 2020, ApJS, 246, 63
- Osherovich, V. A., Fainberg, J., & Stone, R. G. 1999, GRL, 26, 401
- Patsourakos, S., Vourlidas, A., Török, T., et al. 2020, Space Sci. Rev., 216, 131
- Rouillard, A. P., Poirier, N., Lavarra, M., et al. 2020, ApJS, 246, 72
- Savani, N. P., Owens, M. J., Rouillard, A. P., et al. 2011, ApJ, 731, 109
- Thernisien, A. F. R., Howard, R. A., & Vourlidas, A. 2006, ApJ, 652, 763
- Vourlidas, A. 2014, PPCF, 56, 064001
- Vourlidas, A., Howard, R. A., Plunkett, S. P., et al. 2016, Space Sci. Rev., 204, 83
- Vourlidas, A., Lynch, B. J., Howard, R. A., & Li, Y. 2013, Sol. Phys., 284, 179
- Wood, B. E., Hess, P., Howard, R. A., et al. 2020, ApJS, 246, 28
- Wood, B. E., & Howard, R. A. 2009, ApJ, 702, 901
- Wood, B. E., Howard, R. A., & Socker, D. G. 2010, ApJ, 715, 1524
- Wood, B. E., Wu, C. -C., Lepping, R. P., et al. 2017, ApJS, 229, 29